

Two-axis MEMS scanner with transfer-printed high-reflectivity, broadband monolithic silicon photonic crystal mirrors

Jae-Woong Jeong,^{1,2,4,*} Bryan Park,^{1,4} Hohyun Keum,³ Seok Kim,³ John A. Rogers,² and Olav Solgaard¹

¹*E. L. Ginzton Laboratory, Department of Electrical Engineering, Stanford University, Stanford, CA 94305, USA*

²*Frederick Seitz Materials Research Laboratory, Department of Materials Science and Engineering, University of Illinois at Urbana-Champaign, 61801, USA*

³*Department of Mechanical Engineering, University of Illinois at Urbana-Champaign, 61801, USA*

⁴*These authors contributed equally*

jwjeong1@illinois.edu

Abstract: We present a two-axis electrostatic MEMS scanner with high-reflectivity monolithic single-crystal-silicon photonic crystal (PC) mirrors suitable for applications in harsh environments. The reflective surfaces of the MEMS scanner are transfer-printed PC mirrors with low polarization dependence, low angular dependence, and reflectivity over 85% in the wavelength range of 1490nm~1505nm and above 90% over the wavelength band of 1550~1570nm. In static mode, the scanner has total scan range of 10.2° on one rotation axis and 7.8° on the other. Dynamic operation on resonance increase the scan range to 21° at 608Hz around the outer rotation axis and 9.5° at 1.73kHz about the inner rotation axis.

©2013 Optical Society of America

OCIS codes: (220.4000) Microstructure fabrication; (220.4241) Nanostructure fabrication; (230.4685) Optical microelectromechanical devices; (230.5298) Photonic crystals

References and links

1. S. Akiyama, F. J. Grawert, J. Liu, K. Wada, G. K. Celler, L. C. Kimerling, and F. X. Kaertner, "Fabrication of highly reflecting epitaxy-ready Si-SiO₂ Bragg reflectors," *IEEE Photon. Technol. Lett.* **17**(7), 1456–1458 (2005).
2. S. Fan and J. D. Joannopoulos, "Analysis of guided resonance in photonic crystal slabs," *Phys. Rev. B* **65**(23), 235112 (2002).
3. V. Lousse, W. Suh, O. Kilic, S. Kim, O. Solgaard, and S. Fan, "Angular and polarization properties of a photonic crystal slab mirror," *Opt. Express* **12**(8), 1575–1582 (2004).
4. C. F. R. Mateus, M. C. Y. Huang, Y. Deng, A. R. Neureuther, and C. J. Chang-Hasnain, "Ultrabroadband Mirror Using Low-Index Cladded Subwavelength Grating," *IEEE Photon. Technol. Lett.* **16**(2), 518–520 (2004).
5. O. Kilic, S. Kim, W. Suh, Y.-A. Peter, A. S. Sudbø, M. F. Yanik, S. Fan, and O. Solgaard, "Photonic crystal slabs demonstrating strong broadband suppression of transmission in the presence of disorders," *Opt. Lett.* **29**(23), 2782–2784 (2004).
6. W. Suh, M. F. Yanik, O. Solgaard, and S. Fan, "Displacement-sensitive photonic crystal structures based on guided resonance in photonic crystal slabs," *Appl. Phys. Lett.* **82**(13), 1999–2001 (2003).
7. K. B. Crozier, V. Lousse, O. Kilic, S. Kim, W. Suh, S. Fan, and O. Solgaard, "Air-bridged photonic crystal slabs at visible and nearinfrared wavelengths," *Phys. Rev. B* **73**(11), 115126 (2006).
8. Y. Ohira, A. Checkovsky, T. Yamanoi, T. Endo, H. Fujita, and H. Toshiyoshi, "A high-power handling MEMS optical scanner for display applications," in *Proceedings of IEEE/LEOS Conference on Optical MEMS and Nanophotonics* (Institute of Electrical and Electronics Engineers, Freiburg, Germany, 2008), pp. 70–71.
9. G. Brown, G. Thursby, W. Johnstone, and D. Uttamchandani, "MEMS beam steering for high power fiber lasers," in *Proceedings of 4th EMRS DTC Tech. Conference* (Edinburgh, U.K., 2007), B9.
10. E. Stapparts, K. Baker, D. Gavel, S. Wilks, S. Olivier, and J. Brase, "Coherent communications, imaging and targeting," in *Proceedings of IEEE Conference on Aerospace* (Institute of Electrical and Electronics Engineers, 2004), pp. 1105–1116.
11. I. W. Jung, S. Kim, and O. Solgaard, "High-reflectivity broadband photonic crystal mirror MEMS scanner with low dependence on incident angle and polarization," *J. Microelectromech. Syst.* **18**(4), 924–932 (2009).

12. I. W. Jung, S. B. Mallick, and O. Solgaard, "A large-area high-reflectivity broadband monolithic single-crystal-silicon photonic crystal mirror MEMS scanner with low dependence on incident angle and polarization," *IEEE J. Sel. Top. Quantum Electron.* **15**(5), 1447–1454 (2009).
13. S. Hadzialic, S. Kim, A. F. Sarioglu, A. S. Sudbø, and O. Solgaard, "Displacement Sensing With a Mechanically Tunable Photonic Crystal," *IEEE Photon. Technol. Lett.* **22**(16), 1196–1198 (2010).
14. S. Kim, J. Wu, A. Carlson, S. H. Jin, A. Kovalsky, P. Glass, Z. Liu, N. Ahmed, S. L. Elgan, W. Chen, P. M. Ferreira, M. Sitti, Y. Huang, and J. A. Rogers, "Microstructured elastomeric surfaces with reversible adhesion and examples of their use in deterministic assembly by transfer printing," *Proc. Natl. Acad. Sci. U.S.A.* **107**(40), 17095–17100 (2010).
15. T. D. Wang, M. J. Mandella, C. H. Contag, and G. S. Kino, "Dual-axis confocal microscope for high-resolution in vivo imaging," *Opt. Lett.* **28**(6), 414–416 (2003).
16. J.-W. Jeong, S. Kim, and O. Solgaard, "Split-frame gimbaled two-dimensional MEMS scanner for miniature dual-axis confocal microendoscopes fabricated by front-side processing," *J. Microelectromech. Syst.* **21**(2), 308–315 (2012).
17. D.-H. Kim, Z. Liu, Y.-S. Kim, J. Wu, J. Song, H.-S. Kim, Y. Huang, K.-C. Hwang, Y. Zhang, and J. A. Rogers, "Optimized structural designs for stretchable silicon integrated circuits," *Small* **5**(24), 2841–2847 (2009).
18. M. K. Chaudhury and G. M. Whitesides, "Direct measurement of interfacial interactions between semispherical lens and flat sheets of poly(dimethylsiloxane) and their chemical derivatives," *Langmuir* **7**(5), 1013–1025 (1991).
19. C. Harendt, H.-G. Graf, B. Hofflinger, and E. Penteker, "Silicon fusion bonding and its characterization," *J. Micromech. Microeng.* **2**(3), 113–116 (1992).
20. D. Zhao, Z. Ma, and W. Zhou, "Design of dielectric photonic crystal reflector Fabry-Perot cavities," *Proc. SPIE* **7756**, 775610, 775610-9 (2010).
21. C. Ataman and H. Urey, "Nonlinear frequency response of Comb-Driven Microscanners," *Proc. SPIE* **5348**, 166–174 (2004).
22. A. M. Elshurafa, K. Khirallah, H. H. Tawfik, A. Emira, A. K. S. Abdel Aziz, and S. M. Sedky, "Nonlinear dynamics of spring softening and hardening in folded-MEMS comb drive resonators," *J. Microelectromech. Syst.* **20**(4), 943–958 (2011).
23. J. O. Grepstad, P. Kaspar, O. Solgaard, I.-R. Johansen, and A. S. Sudbø, "Photonic-crystal membranes for optical detection of single nano-particles, designed for biosensor application," *Opt. Express* **20**(7), 7954–7965 (2012).

1. Introduction

Optical micro-electro-mechanical systems (MEMS) devices typically employ Aluminum or other metal thin films to enhance reflectivity. Metal mirrors have high, broadband reflectivity, they are compatible with most standard MEMS processes, and, due to their limited thickness, typically less than 100 nm, they do not impart excessive mechanical stress. On the other hand, metal mirrors are fragile; they can handle only modest optical power densities, they have to be hermetically packaged, and they cannot tolerate temperatures above a few hundred degrees. Distributed Bragg reflectors made of dielectric stacks [1] have higher reflectivity than metal mirrors and are much more robust in terms of power handling, chemical resistance, and temperature stability, but they are challenging to incorporate in standard MEMS fabrication processes, and their mechanical rigidity and stress make them incompatible with many optical MEMS devices. Photonic Crystal (PC) mirrors [2–6] retain the high reflectivity and robustness of Bragg mirrors, without the excessive rigidity and stress. 2-D PC mirrors are formed by periodic patterning of high-refractive-index films. High reflectivity over relatively broad optical wavelength is achieved through interference between guided resonances [2] and free-space radiation within the patterned, high-index film. The compact, all-dielectric structure of PC mirrors make them chemically and thermally robust, and enable high optical power handling as well as operation in harsh environment including high temperature. The reflection spectrum of PC mirrors can be engineered from visible to IR wavelengths by manipulating the hole size, pitch, and slab thickness [7]. These unique features make PC mirrors promising for applications such as 3-D displays using laser-induced breakdown plasma [8], high power laser beam steering [9], and coherent communications [10]. High reflectivity MEMS scanners with polysilicon PC mirrors [11], and with monolithic single-crystal-silicon (SCS) PC mirrors [12] have been reported. In these previous reports, the PC mirrors were fabricated directly on the surface of MEMS scanners, increasing the complexity of the fabrication process.

In this paper, we describe a two-axis MEMS scanner with transfer-printed, high-reflectivity, broadband PC mirrors. Stress-free, monolithic PC mirrors were fabricated in a SCS device layer of a silicon-on-insulator (SOI) wafer using GOPHER (generation of photonic element by RIE) process [13], and attached to MEMS scanners using transfer printing [14]. This technique increases design flexibility by allowing optical components with different characteristics to be integrated on a common MEMS platform. Our PC mirrors, designed to be compatible with transfer printing, have higher than 85% reflectivity from 1490 nm to 1505 nm wavelength and higher than 90% reflectivity from 1550nm to 1570nm wavelength. These limits are independent of polarization and angle of incidence, although some polarization and angular dependencies were observed within the bands.

2. Design and fabrication

2.1 Design of two-axis PC mirror MEMS scanner

Transfer printing can be used to integrate PC mirrors on most types of optical MEMS devices. Here, we demonstrate the technique on a two-axis PC mirror MEMS scanner developed for miniature dual-axis confocal microscopes [15]. Figure 1 shows the schematic diagram of our PC mirror MEMS scanner. It is comprised of a dogbone-shaped scanner with two PC reflectors, self-aligned electrostatic combdrive actuators, and outer and inner springs for 2-D scanning. The scanner base, movable combdrives, and inner torsional springs are located in the bottom device layer. The fixed combdrives and outer torsional springs are made in double-stacked SOI. The dimensions of outer springs are $5\mu\text{m} \times 250\mu\text{m} \times 45.3\mu\text{m}$ in width, length, and thickness. The inner springs are folded three times, and the dimensions of transverse and longitudinal components are $4\mu\text{m} \times 70\mu\text{m} \times 25\mu\text{m}$ and $4\mu\text{m} \times 70\mu\text{m} \times 25\mu\text{m}$, respectively. The combdrives have $5\mu\text{m}$ -wide comb fingers and $5\mu\text{m}$ - and $4\mu\text{m}$ -gaps for the outer and inner combdrives, respectively.

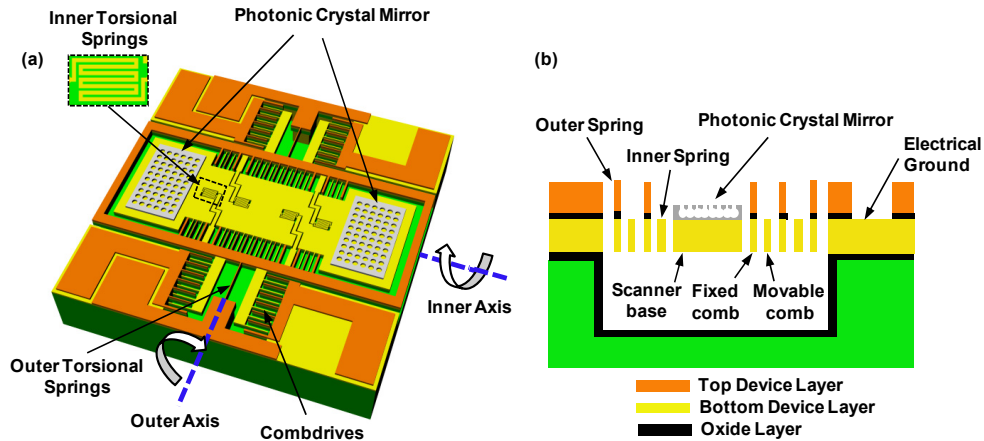


Fig. 1. Two-axis PC MEMS scanner (a) Schematic diagram, (b) Cross-sectional diagram.

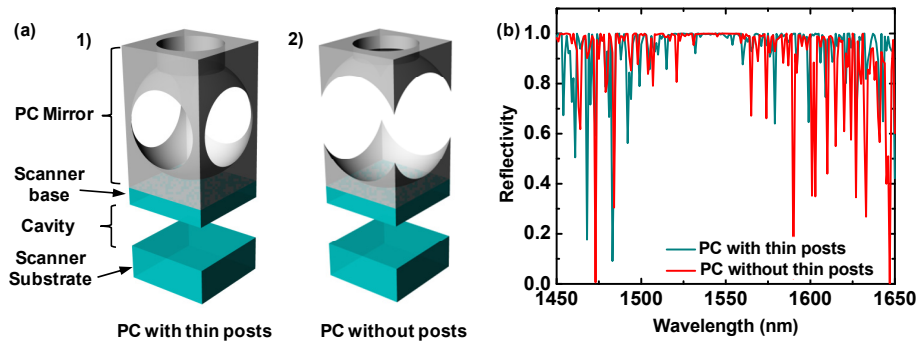


Fig. 2. (a) Simulation structures 1) with and 2) without thin posts (not to scale) (b) Reflection spectrum simulation of PCs with and without thin connecting posts.

Two separate PC mirror islands are transfer-printed onto two separate rectangles ($400\mu\text{m} \times 600\mu\text{m}$ in area) of the scanner base. Each island consists of a $300\mu\text{m} \times 300\mu\text{m}$ PC area and additional $25\mu\text{m}$ margins on all four sides where the microtips of a PDMS stamp are applied during the transfer printing process. The PCs are two-dimensional SCS membranes with a square lattice of air holes. The 90-degree rotational symmetry makes the reflection of the PC mirrors independent of polarization for normal incidence. We use Rigorous Coupled Wave Analysis (RCWA) simulations to determine the PC parameters – hole diameter and membrane thickness – that lead to broadband reflectivity around 1550nm . Large holes and thin diaphragms are required for broadband mirrors because strong scattering and coupling lead to short lifetime of the guided resonances in the PCs [6]. The period of the PC is fixed at $1\mu\text{m}$ and the hole diameter is varied around 70-80% of the period and the thickness around 50-65%. In our practical implementation, the PC membranes are partially released from the Si substrates using an isotropic etch so that thin posts connect them at the corners of the square lattice. The remaining posts add structural robustness without sacrificing optical performance, allowing for a reliable transfer process.

Figure 2 shows the PC structures used in the RCWA simulations and simulated reflection for two PCs with and without the thin connecting posts. Each structure is comprised of a GOPHER PC on the SCS scanner base suspended with an air gap on the SCS scanner substrate. The PC is modeled as a cylindrical hole terminated in a spherical hole centered on a square unit cell. The thicknesses of the scanner base and the air gap are extracted from the measurements as explained in the section 3. Our simulations are carried out with a plane wave normally incident on the structure. The two simulations in Fig. 2(b) share the same PC dimensions of pitch = $1\mu\text{m}$, hole diameter = 700nm , and membrane thickness = 650nm , but differ in the sphere radii, which are 700nm and 800nm for the partial and complete released PCs respectively. The simulation results show clearly that the presence of the posts has negligible impact on the broadband reflectivity region around 1550nm .

2.2 Fabrication

The detailed fabrication process of the MEMS scanner has been described previously [16]. The PC mirrors are fabricated on a SOI wafer by using the GOPHER process as shown in Fig. 3(a). The SOI wafer has $3\mu\text{m}$ -thick SCS device layer on $1\mu\text{m}$ -thick buried oxide (BOX) layer. First, the wafer is thermally oxidized to form 500nm -thick hard etch mask. Then, we use an ASML i-line stepper to define the PC pattern with photolithography. The pattern is transferred to the oxide mask and the device layer by reactive ion etching (RIE). Then, we cover the wafer with $1.6\mu\text{m}$ -thick photoresist (SPR3612) and expose it to leave $350\mu\text{m} \times 350\mu\text{m}$ square aligned on the previously etched PC patterns. A deep RIE removes all the exposed SCS device layer and the PC mirror islands are formed on the BOX layer. After a 60nm -thick sidewall oxidation, the oxide at the bottom of the PC holes is etched by RIE.

Subsequently, another Si anisotropic etch extends the holes into the device layer, and an SF₆ isotropic undercut etch is performed until the PC membrane is connected to the underlying device layer only with thin posts at the center of the diagonal between holes.

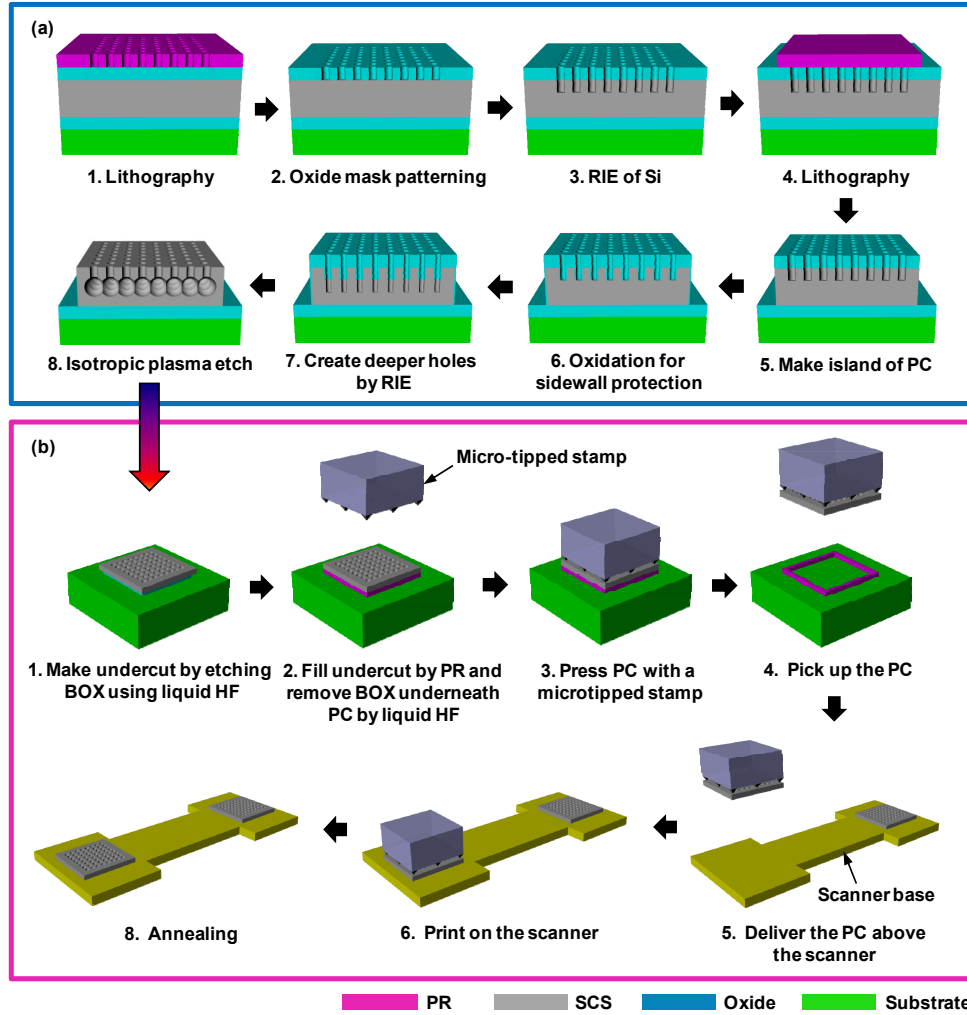


Fig. 3. Schematic diagram of (a) PC fabrication and (b) transfer-printing process (not to scale).

Figure 3(b) shows the transfer process of the PC mirrors. Timed HF etching creates undercut at the border of PC islands. Photoresist (AZ5214) is spin-coated, UV-exposed without a mask, and developed to remove all the photoresist except in the undercut area. By immersing the sample in liquid HF, the buried oxide is removed and the PC units are suspended on the photoresist. A PDMS microtipped stamp is used to pick up and print PC mirrors on the surface of the scanner. The microtips of a stamp should have a minimum height to achieve sufficient restoring force to restore the microtips back to their original geometry after mechanical collapse. The minimal height can be expressed as [14],

$$h_{\min} = \sqrt{\frac{w_{\text{stamp}}\gamma}{\bar{E}} \left[3.04 \ln \left(\frac{w_{\text{stamp}}\bar{E}}{\gamma \tan^2 \frac{\theta}{2}} \right) - 11.5 \right]} \quad (1)$$

where w_{stamp} is a microtip spacing. The plane-strain modulus (\bar{E}) of PDMS is 2.4MPa when Poisson's ratio is 0.5 [17], the work of adhesion (γ) between PDMS and Si is 155mJ/m² [18], and θ is 90°. In this work, the height of the microtips is 8.1 μm with $w_{\text{stamp}} = 48\mu\text{m}$. A contact mask aligner (Karluss MJB3) is used for the stamping process. The microtipped stamp is mounted on a blank mask glass, and the scanner and the PCs are loaded into the aligner so that precise alignment can be achieved for both pick-up and printing. When the stamp is pressed with high preload (40mN), the regions between the microtips of the stamp collapse, maximizing the contact area and thus the adhesion force. Upon the collapse of the microtips, the stamp is quickly retracted to make an even larger adhesion force against the PC through viscoelastic effect [14]. The retrieval is a purely mechanical process, which does not require any heat or chemical treatment. The adhesion force between the stamp and the PC is larger than the force between the PC and photoresist, thus resulting in breakage at the interface between the photoresist frame and the PC. In most cases, there is negligible photoresist residues remaining on the retrieved PC, and therefore, no further cleaning is required. However, even if there is some photoresist remaining on the PC, the organic compound is burned and removed during the annealing process to permanently bond the PC to the scanner. After picking up the PC, the microtipped stamp is restored to its original form due to its elastic stiffness, making a minimal contact with the PC. Therefore, the PC mirror can be released upon printing on a released MEMS scanner (preload = 4mN), which has a larger contact area. Finally, fabrication is finished by forming covalent bonding between the scanner and PC mirrors through an annealing process at 900°C for five minutes. After covalent Si-Si bonding, the bonding strength is presumed to be similar to the known Si fusion bonding strength of 2.6J/m² [19]. The high melting temperature of Si (1414 °C) and SiO₂ (1600 °C) allows the all dielectric device to be used in high temperature and/or high power applications. The SEM images of the completed PC mirror MEMS scanner is shown in Fig. 4.

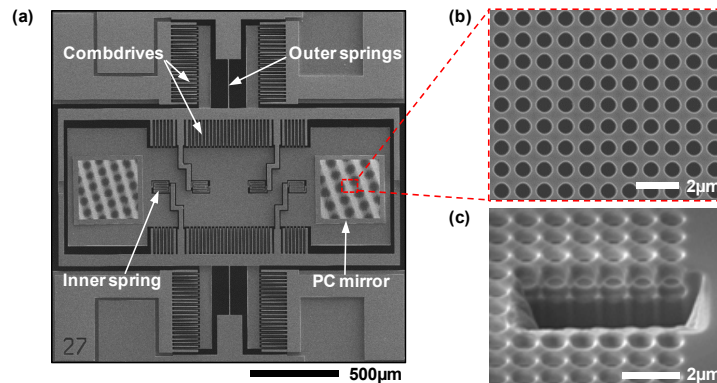


Fig. 4. SEM Images of the PC mirror MEMS Scanner (a) Full device view; the check patterns on PC mirrors are due to the electron beam diffraction, (b) Top view of the PC mirror, (c) Cross-sectional view of the PC mirror.

3. Characterization of PC mirror MEMS scanners

The optical measurement setup for characterization of the PC mirror on MEMS scanner is shown in Fig. 5. For PC reflection spectral measurements, an Erbium-doped fiber amplifier (IPG Photonics EAD-500-C) is used to emit broadband light from 1450nm to 1650nm. The output beam is fiber-coupled to a single mode fiber and goes through a collimator and a linear polarizer for s/p-polarization control. The beam is focused onto the sample by a lens, and a nonpolarizing beam splitter (BS2) collects the reflected light. The focused beam on the sample can be approximated as a Gaussian beam, and the angular distribution within the beam affects the PC reflection response by decreasing the depth of the guided resonances and broadening them [7]. However, the spot size of 40 μm on the sample corresponds to the small

divergence angle of $\sim 1.4^\circ$, and therefore the beam can be regarded as collimated in our setup. In addition, the broadened resonances have small impact on PC mirror operation; the angular components in the input beam are reflected at almost the same reflectivity in the broadband high reflectivity region [3]. As a result, the focused beam can be safely used to measure the PC mirror response, and the beam profile also does not change noticeably after the reflection. Light from an illuminator (Fiber-Lite MI-152) is coupled into the system using another nonpolarizing beam splitter (BS1) and illuminates the sample for viewing and positioning the focused beam onto a desired location on the sample, using a steering mirror to direct the reflected light to an IR-camera. For spectral measurements, the steering mirror is removed, and the reflected beam is coupled into an optical spectrum analyzer. The PC reflection spectrum is calibrated by comparison to the 97.5% reflectivity silver mirror (Thorlabs PF03-03-P01).

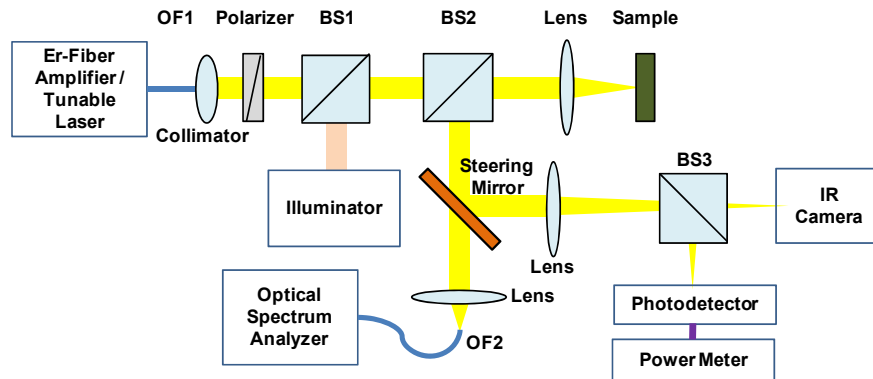


Fig. 5. Optical setup for the PC mirror MEMS scanner reflectance measurement. OF1 and 2: single mode optical fibers, BS1~3: beam splitters. The steering mirror can be removed to couple light into the optical spectrum analyzer.

Because the MEMS scanner is composed of a SCS scanner base, an air gap, and a SCS substrate (Fig. 1), its reflection spectrum exhibits multiple Fabry-Perot resonances corresponding to the thickness of $24\mu\text{m}$ and $480\mu\text{m}$ for the SCS scanner base and the air gap, respectively (Fig. 6(a)). However, the PC mirror-mounted scanner shows two broadband high reflectivity regions around 1500nm and 1550nm each with significantly decreased Fabry-Perot effect as shown in Fig. 6(b). The Fabry-Perot effect from the PC mirror and the scanner base appears in the second region as small dips while the Fabry-Perot effect from the air gap are not observed in the spectrum. The minimized Fabry-Perot appearance is due to high reflectivity of the PC mirror and the increased light scattering from the GOPHER-generated scallops under the PC membrane. The Deep RIE process also roughens the bottom surface of the scanner base, leading to increased scattering. The measured free spectral range of the small dips is $\sim 10\text{nm}$, which corresponds to a $34\mu\text{m}$ -thick uniform silicon slab. The combined thickness of the PC mirror island and the scanner base is $27\mu\text{m}$. This discrepancy is caused by the fact that the GOPHER PCs give rise to phase delays upon reflection so that effective cavity length becomes longer [20]. The overall reflection level from the measurement is lower than the simulated value because of the fabrication errors such as sidewall slope in PC profile and ellipticity in the GOPHER isotropic release. The PC spectrum in Fig. 6(b) also shows polarization dependence. For the s-polarization, the reflectivity is over 90% in the wavelength ranges of $1490\sim 1520\text{nm}$ and $1540\sim 1570\text{nm}$. The second band has two sharp reflectivity drops to 80% in the vicinity of 1546nm and 1556nm due to the Fabry-Perot effect. For the p-polarization, the reflectivity is above 85% in the $1490\sim 1505\text{nm}$ range and above 90% over $1550\sim 1570\text{nm}$ with sharp Fabry-Perot modulation at 1548nm and 1557nm , which brings the reflectivity down to 75% locally. This polarization dependence is caused by the fact that the

PC holes are not perfectly four-fold symmetric. However, the polarization dependence is small in the high reflectivity region centered at 1550nm. The angle dependence of the PC mirror is measured at 1567nm which is the peak reflectivity wavelength in that band. The definition of incidence angle and azimuthal angle is shown in Fig. 6(c). In the setup, the incidence angle is changed up to 5° by shifting the position of the focusing lens in front of the sample. At each incidence angle, the azimuthal angle is changed by rotating the sample holder at $0\sim 45^\circ$ with respect to one of the PC lattice directions. The input source is switched to a tunable laser (New Focus 6427) emitting 1567nm-wavelength light and the reflected power from the PC mirror is directed to a photodetector (Newport 818-IR) and a power meter (Newport 1815-C) as shown in Fig. 5. The measured angular dependencies of the s- and p-polarizations are presented in Fig. 6(d). Regardless of the polarization state, the mirror has very low azimuthal angle dependence and maintains its high reflectivity over 85% with less than 10% variation up to $\pm 3^\circ$ incident angle change. The scan angle is twice as large as the variation in incident angle, so this corresponds to a scan angle tolerance of 12° , which is large enough for most applications including the dual-axis confocal microscope [15].

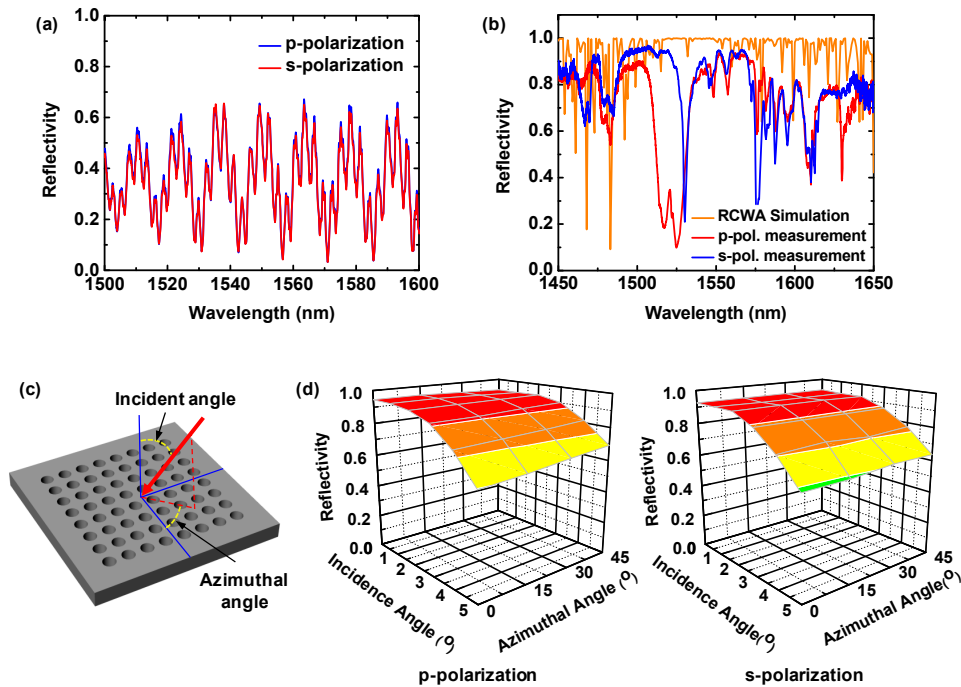


Fig. 6. Optical measurement of the PC mirror MEMS scanner (a) Reflection spectrum of the silicon mirror of the scanner (b) Reflection spectrum of the PC mirror MEMS scanner (c) Definition of incident and azimuthal angle with respect to the PC mirror (d) Angular dependence of the PC mirror MEMS scanner at p- and s-polarization.

The surface profile of the scanner base and the PC mirror are measured by a WYKO white light interferometer (NT1100) as shown in Fig. 7. Our measurement shows that the scanner base mirror has a radius of curvature of 12m, ensuring a very flat surface for PC printing. The peak-to-valley surface deformation of the PC mirror is 60 nm, which is smaller than $\lambda/25$. This excellent flatness is anticipated from PC mirrors fabricated in stress-free SCS. The roughness of the PC mirror was measured using an atomic force microscope (Park Systems XE-70). The root-mean-square roughness of the mirror surface excluding air holes is measured over the area of $400\text{nm} \times 400\text{nm}$ and the value is 1nm, which ensures good optical quality.

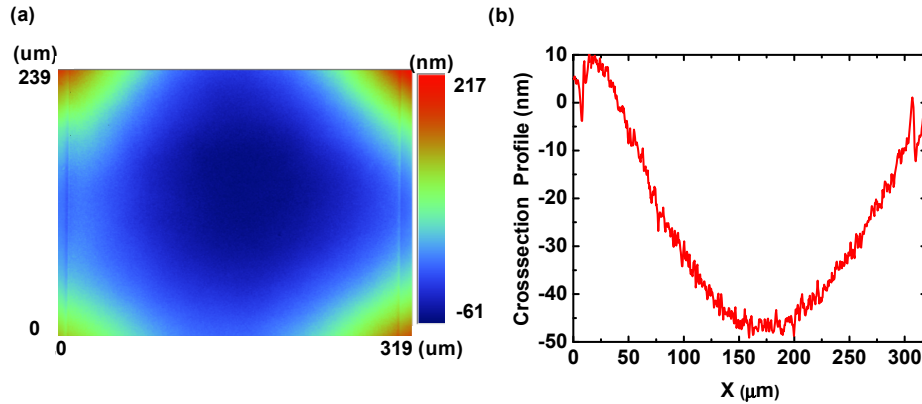


Fig. 7. (a) Surface profile of the transferred PC mirror. (b) Cross section across the center showing a peak-to-valley value of ~ 60 nm ($320 \mu\text{m}$ in length) resulting in a flatness of $\lambda/25$.

The scanner performance was characterized before and after transfer printing of the PC mirrors. For the testing, aluminum wires were bonded directly on the Si electrode pads. Our PC mirror has a mass of ~ 500 nano-gram, which negligibly affects the performance of the MEMS scanner. This was verified by measurements of optical deflection angle in both static and dynamic operation after PC transfer printing. The static measurement results in Fig. 8(a) show that the optical deflection angles range from -5.17° at $V_2 = 140\text{V}$ to 5.11° at $V_1 = 140\text{V}$ for the outer axis and from -3.94° at $V_4 = 70\text{V}$ to 3.87° at $V_3 = 100\text{V}$ for the inner axis. The optical deflection in dynamic mode was measured using a position sensitive detector. When driving voltages of $(61 + 48\sin\omega t)\text{V}$ and $(46 + 73\sin\omega t)\text{V}$ are applied for the outer and inner axes, respectively, small resonant frequency shifts were observed for both axes after PC bonding – from 614Hz to 608Hz for the outer axis and from 1.74kHz to 1.73kHz for the inner axis. The optical deflection angles at the torsional resonance frequency reached $\pm 10.49^\circ$ for the outer axis and $\pm 4.77^\circ$ for the inner axis after PC bonding (Fig. 8(b)). In addition to the fundamental torsional resonance frequency of f_0 , sub-harmonic modes at $f_0/3$ and $f_0/2$ for both axes, and second harmonic at $2f_0$ for the outer axis are observed. These modes are likely caused by the nonlinear voltage response of the combdrive actuators [21]. The asymmetric peaks with a sharp decrease of the amplitude at harmonics and sub-harmonics of the resonance frequency appear due to the spring hardening effect [22]. Due to strong covalent bonding between the PC mirrors and the scanner base, the PC mirrors are remained attached in high speed operation at the resonant frequencies.

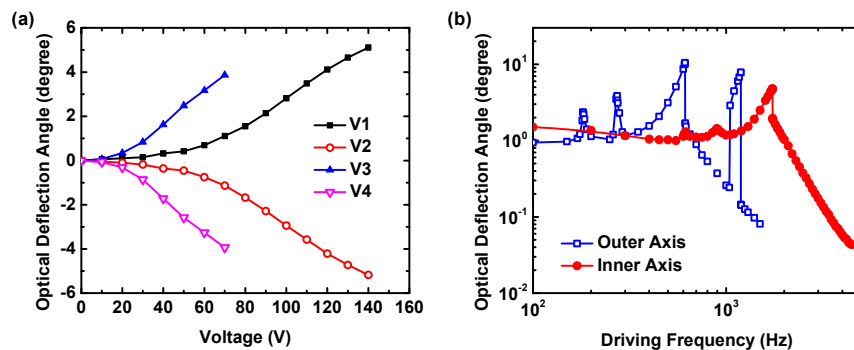


Fig. 8. Optical deflection curves after PC bonding in (a) Static mode – V_1 and V_2 are for the outer axis, and V_3 and V_4 are for the inner axis, (b) Dynamic mode.

4. Conclusion

A two-axis electrostatic MEMS scanner with PC mirrors has been developed using a transfer-printing technique. The PC mirror MEMS scanner shows broadband high-reflectivity with low angular and polarization dependence. The good optical performance and robust, all-dielectric construction of the PC MEMS scanner, makes it a candidate for applications that require high optical power handling and/or operation in harsh environments. Operation in different wavelength ranges can be achieved by scaling the dimension of PC mirrors to match the requirements and, if necessary, different materials can be used to avoid absorption, e.g. at visible wavelengths, large-bandgap dielectric materials with high refractive index such as silicon nitride film can be used [7,23] Furthermore, the combination of nanophotonic devices and MEMS with transfer printing enables flexible design and we expect that it will lead to development of devices with improved functionality.

Acknowledgments

Jae-Woong Jeong and Bryan Park contributed equally to this work. The authors thank Xuan Wu and Antonio Gellineau for his RCWA software implementation. This work was sponsored by the Boeing Company under contract #33130.